




Cite this: *Phys. Chem. Chem. Phys.*,
2025, 27, 14526

Ni²⁺ induced high ferromagnetic ordering and dielectric relaxation phenomena in KBiFe₂O₅ brownmillerite†

Payala Sahoo,^a Sujata Kumari Ray,^a Anupama Pati,^a A. K. Sahoo,^a Jaspreet Singh^b
and S. Dash ^{*a}

This work primarily focuses on the high ferromagnetic ordering and dielectric relaxation mechanism in KBiFe₂O₅ brownmillerite owing to the substitutions of Ni, which is otherwise a canted antiferromagnetic system. A nominal composition of KBiFe_{2-x}Ni_xO₅ ($x = 0, 0.025, 0.05$, and 0.1) was synthesized via a solid-state method, and a single phase with monoclinic structure (space group-*P2₁/c*) of the series was probed through X-ray diffraction. X-ray photoelectron and Mössbauer spectroscopies predicted a mixed valence state of Fe (Fe²⁺ and Fe³⁺). Thermomagnetic studies revealed an antiferromagnetic transition in the parent system, while Ni substitution resulted in a ferromagnetic transition at around 815 K. The thermomagnetic irreversibility predicted a cluster glass-like state well below the room temperature, which could be associated with the phase competition among the two phases of contrasting order. Isothermal magnetization revealed a ferromagnetic ordering in Ni-substituted KBiFe₂O₅, with a fifteen-fold increase in the room-temperature magnetic moment compared with that of the parent compound. This drastic change in the magnetization is analysed in the framework of lattice distortion and change in the tilting angle of Fe³⁺–O^{2–}–Fe³⁺ chain due to Ni²⁺ along with the exchange interactions among Ni²⁺, Fe³⁺ and Fe²⁺ ions in the system. Furthermore, a dielectric transition was observed at around 753 K, which hardly changed with Ni substitution. The tangent loss and electric modulus studies demonstrated a relaxation behavior, and the relaxation peaks were shifted towards lower frequencies with Ni substitution with an increase in activation energy. The improved magnetic and electrical characteristics make these materials potential candidates for multifunctional applications.

Received 2nd April 2025,
Accepted 12th June 2025

DOI: 10.1039/d5cp01267h

rsc.li/pccp

1. Introduction

Multiferroics are a special class of materials, which are popular among the scientific community for their rarity and unique properties.^{1–4} In multiferroics, the mutual control of magnetic ordering (or polarization) by an electric field (or magnetic field) significantly enhances their applicability towards multifunctional device fabrications.^{1–4} These materials are even more fascinating as they necessitate the coexistence of two contrasting order parameters (ferroelectricity and magnetic order) in a single phase. In this class of multiferroics, brownmillerites are of great interest as it owns a rich amount of physics along with a wide applications in different fields, such as magnetic

storage, magnetic field sensors, high energy capacitors and solar cells.^{5,6} The general form of brownmillerites A₂B₂O₅ (A: K, Ca, Ba, and Bi; B: Fe, Al, and In) mostly consists of an alternate stacking of tetrahedral (BO₄) and octahedral (BO₆) layers. Among these, KBiFe₂O₅ is a unique compound owing to the simultaneous presence of polar (Curie temperature, $T_C \sim 773$ K) and magnetic ordering (Néel temperature, $T_N \sim 560$ K) above room temperature.⁷ Structurally, the single crystal KBiFe₂O₅ is orthorhombic, while the monoclinic phase of this compound has also been reported by several groups.^{7,8} Interestingly, the KBiFe₂O₅ structure contains only FeO₄ tetrahedra, unlike other brownmillerites, and it is notable that tetrahedral materials are more covalent owing to the shorter bond lengths of Fe–O. KBiFe₂O₅ typically exhibits a weak ferromagnetic (WFM) ordering, which is linked to the canting of the uncompensated antiferromagnetic (AFM) spins of Fe³⁺ ions (high spin state), in which the spin structure is found to be incommensurate with the crystal structure.^{7,9,10} However, the exact reason for the weak ferroelectricity of this system is still under intense scrutiny. It may be associated with the small displacement of K⁺ and Bi³⁺ in

^a Department of Physics and Astronomy, National Institute of Technology, Rourkela, Odisha-769008, India. E-mail: dsuryanarayan@gmail.com

^b Technical Physics Division, Bhabha Atomic Research Center, Mumbai 400085, India

† Electronic supplementary information (ESI) available. See DOI: <https://doi.org/10.1039/d5cp01267h>

the non-centrosymmetric single crystal ($1.47 \mu\text{C cm}^{-2}$)¹¹ or due to the presence of a lone pair of Bi^{3+} in an otherwise centrosymmetric form of KBiFe_2O_5 .¹²

However, a very low magnetic moment acquired by KBiFe_2O_5 limits its applicability in device applications. Few attempts have been made to improve its magnetization either by suitable chemical substitutions at different sites or adopting other synthesis processes. A partial substitution of La^{3+} and Y^{3+} at the Bi^{3+} site improved both the magnetic and optical properties; however, magnetic saturation was not achieved in a moderate field of 1.5 T.^{13,14} On the other hand, Ho^{3+} and Co^{3+} doping at the Bi^{3+} and Fe^{3+} sites enhanced the magnetic moment due to the development of WFM ordering, along with the dominance of canted AFM ordering.^{12,15} Similarly, orthorhombic KBiFe_2O_5 nanoparticles were also synthesized, which exhibited a superparamagnetic behavior.¹⁶ Although several works have also focused on other physical properties, for most device applications, a high saturation magnetic moment is a prerequisite for a system with magnetism over a wide temperature range, which is rare in the case of KBiFe_2O_5 . In this context, since Ni^{2+} is a magnetic ion, KBiFe_2O_5 is expected to exhibit an interesting response to magnetic fields and temperature, in which ferromagnetic ordering may dominate over the canted AFM state and subsequently alter the magnetic transition towards higher temperatures. The incorporation of Ni in KBiFe_2O_5 can effectively modulate magnetic transition, leading to the convergence between the T_N and T_C . To the best of our knowledge, Ni substitution in KBiFe_2O_5 brownmillerite and the subsequent drastic change in the room temperature magnetic moment have rarely been reported in the literature. With Ni^{2+} substitutions at the Fe^{3+} site, the dielectric relaxation is also studied using a detailed electric modulus and dielectric loss analysis. This work primarily aims to investigate the influence of a magnetic ion, Ni^{2+} , on the structural, magnetic and dielectric response properties of KBiFe_2O_5 brownmillerite.

2. Experimental methods

Polycrystalline samples of $\text{KBiFe}_{2-x}\text{Ni}_x\text{O}_5$ ($x = 0, 0.025, 0.05, 0.1$) were synthesized using a conventional solid-state reaction method in which high purity chemicals Fe_2O_3 ($\geq 95\%$, Himedia), Bi_2O_3 ($\geq 99\%$, Himedia), K_2CO_3 ($\geq 99\%$, Emplura), and NiO ($\geq 99.9\%$, Molychem) were used as precursors. Stoichiometric amounts of these oxides were mixed and ground in an agate motor and pestle in an acetone medium for 5 hours. Consequently, the ground powder was calcined at 700°C for 4 hours, and after natural cooling to room temperature, the calcined powder was reground and pressed into circular-shaped pellets. Subsequently, the pellets were sintered at the same temperature for 2 hours in the air medium. These pellets were again ground thoroughly to achieve a better crystallinity of the samples.

For determining phase purity, X-ray diffraction (XRD) (Empyrean: multi-functional X-ray diffraction system, M/s. Malvern Panalytical) of the samples was carried out at room temperature with $\text{Cu K}\alpha$ -1.54 Å radiation. The microstructural properties of the samples were investigated using a scanning

electron microscope (SEM) (JEOL JSM-6480 LV). The X-ray photoelectron spectroscopy (XPS) measurement was performed using synchrotron radiation with an incident energy of 4065 eV. The survey spectra and high-resolution spectra were recorded at a step size of 0.5 eV and 0.1 eV, respectively, using a pass energy of 120 eV and 180 eV. For a clear understanding of the oxidation and magnetic states of the samples, room-temperature Mössbauer measurements were carried out in transmission mode using a ^{57}Co radioactive source and in a constant acceleration mode using a Mössbauer spectrometer equipped with a Weissel velocity drive. The high and low T magnetic measurements (M - H) of the samples were obtained using a vibrating sample magnetometer (Lakeshore 7040 and 7410). The AC-susceptibility measurement was carried out using a SQUID-VSM-based MPMS system (M/s Quantum Design, USA). The impedance and modulus spectra were recorded with an IM-3570 impedance analyzer integrated with a customized high-temperature dielectric cell. To examine the optimal performance of the experimental setup, impedance and dielectric measurements were performed on a commercial BaTiO_3 and CCTO single crystal, yielding values similar to those reported in the literature. The $\text{KBFe}_{2-x}\text{Ni}_x\text{O}_5$ ($x = 0, 0.025, 0.05$, and 0.1) samples are abbreviated as KBFN0, KBFN2.5, KBFN5 and KBFN10, respectively, unless stated otherwise.

3. Results and discussions

3.1 Structure and surface morphology analysis

The crystal structure and phase purity of KBFN0-10 are detected using room-temperature XRD patterns of the powders, as shown in Fig. 1(a)–(d).

A comprehensive analysis of the structure as well as phase purity is performed through Rietveld refinement using Fullprof software (Fig. 1(a)–(d)). All the samples were found to crystallize in a monoclinic structure with a $P2_1/c$ space group. The structural parameters extracted from the Rietveld refinement are listed in Table 1. Fig. 1(e) shows the schematic diagram (using the VESTA tool) of the monoclinic unit cell structure of KBFN5, with stacking of FeO_4 tetrahedra and corner-sharing BiO_6 octahedra. Fig. 1(f) shows the FeO_4 tetrahedra chain of KBFN5 tilting along the (001) direction. The tetrahedral tilting angle (Φ_T/Θ_T) can be obtained by $\Phi_T/\Theta_T = (180 - \Phi_T/\Theta_T)/2$.¹⁷ The tilting angles are also listed in Table 1. The increasing tilting angles and tetrahedral distortion with Ni substitution are expected to influence the magnetic properties. When the Ni^{2+} ion substitutes Fe^{3+} , it creates a local strain or lattice distortion in the lattice due to the ionic radius mismatch. Therefore, the FeO_4 tetrahedra tilt to adjust the crystal structure or maintain stability, which results in the Fe–O–Fe tilting angle increasing with Ni doping. BiO_6 octahedra are also depicted in the inset of Fig. 1(a). The unit cell parameters are marginally increased with increasing Ni concentration compared to the parent compound, leading to an expansion of the cell volume due to the larger ionic radius of the dopant Ni^{2+} (0.69 Å) ion compared to the host Fe^{3+} (0.55 Å) ion. The average crystallite size (D) is calculated using the Scherrer formula,¹⁸ $D = K\lambda/\beta \cos \theta$, where K

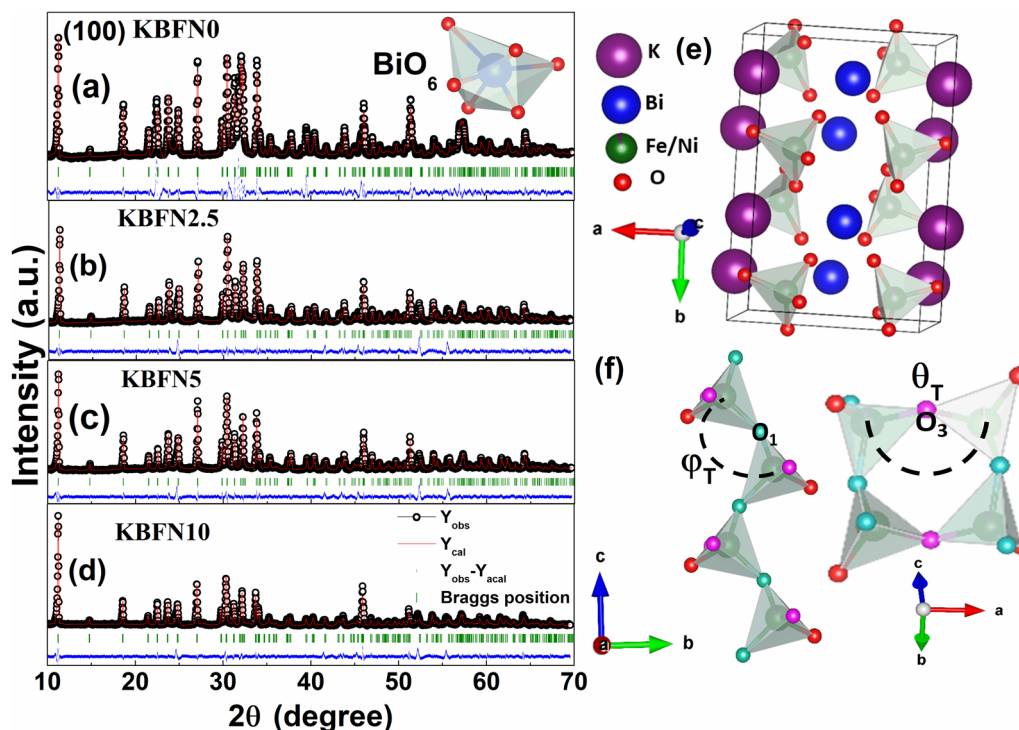


Fig. 1 (a)–(d) Rietveld refinement of XRD patterns of KBFN0–10, (e) schematic of the unit cell structure of KBFN5 and (f) schematic of tilting of FeO_4 tetrahedra along the c axis, inset of (a): BiO_6 octahedra.

Table 1 Structural parameters of KBFN0–10

$\text{KBiFe}_{2-x}\text{Ni}_x\text{O}_5$	$x = 0.0$	$x = 0.025$	$x = 0.05$	$x = 0.1$
a (Å)	7.9124(3)	7.9170(2)	7.9114(5)	7.9286(2)
b (Å)	5.9764(5)	5.9870(4)	5.9828(3)	5.9997(7)
c (Å)	5.7300(3)	5.7371(6)	5.7337(4)	5.7489(6)
V (Å ³)	270.95	271.93	271.38	273.47
D (nm)	52	53	55	59
R_p	18.1	18.6	18.7	19.8
R_{wp}	21.0	18.9	18.4	19.4
β (°)	94.44	94.45	94.46	94.48
$\langle \text{Fe–O} \rangle$ (Å)	1.74	1.78	1.86	1.91
$\angle \text{Fe–O}_1\text{–Fe}$ (°)	168.02(8)	154.54(5)	144.25(7)	142.23(9)
$\angle \text{Fe–O}_3\text{–Fe}$ (°)	149.77(18)	148.33(9)	141.96(11)	140.35(3)
Φ_T (°)	5.99	12.73	17.87	18.88
Θ_T (°)	15.11	15.83	19.02	19.82

is the shape parameter and taken as 0.9, λ denotes wavelength of the source (0.154 nm), and β is the full-width half maximum of the Bragg peaks. The D value is found to increase from 52 nm to 59 nm with increasing Ni concentration.

To further investigate the surface morphology, SEM analysis is performed for KBFN0–10. Fig. 2(a)–(c) shows the SEM images of a few representative samples, and it is observed that the grains are arranged in an irregular manner. The average grain size is calculated using the histogram of grain size distributions (inset of Fig. 2(a)–(c)) and ImageJ software and found to increase from 1.58 μm to 1.97 μm with increasing Ni substitution. The increase in grain size occurs when a foreign atom is doped into a crystal lattice, leading to lattice distortion and acting as a nucleation site for grain growth. To confirm the

exact level of substitutions in the compound, an elemental analysis is carried out using the EDX spectra of all the samples. For conciseness, the EDX spectra of KBFN10 are shown in Fig. 2(d), and the spectra for the rest of the samples are included in ESI† Fig. S1(a)–(c). It is found that all the elements, including K, Bi, Fe, Ni and O, are present in near-stoichiometric proportions within the experimental limit in the samples.

3.2 XPS and Mössbauer spectral analysis

To decipher the role of Ni substitution on the chemical states of KBFN0, XPS measurement was performed at room temperature. Fig. 3(a)–(g) shows the high-resolution spectra of all the elements in the samples, where the core-level binding energies are calibrated with respect to the C 1s peak (285 eV) and analyzed using CasaXPS software. All the spectra are deconvoluted and fitted with a Lorentzian–Gaussian shape to determine the chemical states of all elements. As shown in Fig. 3(a)–(d), the Fe 2p spectra of all the samples consist of two peaks, Fe 2p_{1/2} and Fe 2p_{3/2}, due to spin–orbit coupling. In particular, for KBFN10, the peaks at 711.01 eV and 724 eV correspond to Fe 2p_{3/2} and Fe 2p_{1/2} of the Fe^{3+} state, respectively, with an energy difference of 13.42 eV, whereas the peaks at 709.76 eV and 723.16 eV are assigned to Fe 2p_{3/2} and Fe 2p_{1/2} of the Fe^{2+} state, respectively.¹⁹ However, in the parent compound, Fe exists in only +3 oxidation state (Fig. 3(a)). The progressive increase in the Fe^{2+} content with Ni suggests charge compensation through the reduction of Fe^{3+} to Fe^{2+} . Furthermore, the ratio between the Fe^{3+} and Fe^{2+} states are 4.01, 3.12 and 2.36 for KBFN2.5, KBFN5 and KBFN10, respectively. The satellite peaks are also

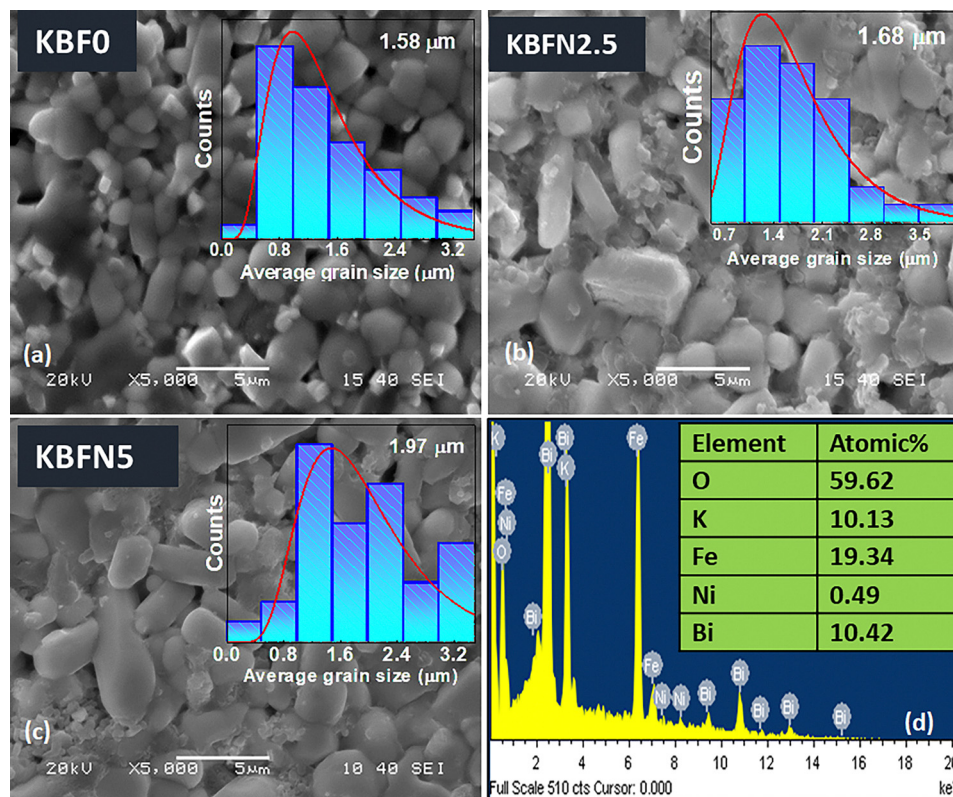


Fig. 2 (a)–(c) Surface morphology for KBFN0–5 and (d) EDX spectra of KBFN5. Inset: (a)–(c) grain size distributions.

distinguished at the binding energies of 717.8 eV and 730.7 eV, corresponding to $2p_{3/2}$ and $2p_{1/2}$, respectively, which usually arise owing to the shake-up process during the ejection of photoelectrons from the 2p orbital; a little amount of kinetic energy is lost inevitably stimulating the movement of electrons from the 3d orbital to the empty 4s orbital.

As shown in Fig. 3(e), the Ni 2p main spectrum is split into two peaks, Ni $2p_{3/2}$ and Ni $2p_{1/2}$, due to spin–orbit coupling. These two peaks and the corresponding satellite peaks of Ni $2p_{3/2}$ and Ni $2p_{1/2}$ are observed at binding energies of 853.9 eV, 871.8 eV, 860.1 eV and 870.8 eV, respectively. In addition, the energy difference between Ni $2p_{3/2}$ and Ni $2p_{1/2}$ is 17.9 eV, which corresponds to the +2 oxidation state of Ni. The Fe 2s peak is also integrated with the Ni 2p spectra and visualized at a binding energy of 848.4 eV. As shown in Fig. 3(f), the O 1s spectrum is deconvoluted into three peaks on account of the different chemical environments of the oxygen anion. The peak at the binding energy of 529.4 eV is ascribed to the metal–oxygen bond (lattice oxygen) in the compound, the peak at 531.1 eV corresponds to the characteristic peak of O^{2-} absorption at the surface and the binding energy of 533.1 eV is as a result of hydroxyl (OH^-) ion or H_2O content in the sample. From Fig. 3(f), the Bi 4f spectra comprise two peaks, $4f_{5/2}$ and $4f_{7/2}$, at the binding energy of 163.5 eV and 158.2 eV, respectively,²⁰ a prototypical spectrum of Bi^{3+} . The Bi 4f spectra for all samples are shown in Fig. S2(a)–(d) (ESI[†]). The K 2s spectra of KBFN0–10 are given in Fig. S2(e)–(h) (ESI[†]). An intense peak is observed at ~ 377.10 eV for KBFN10, which corresponds to the +1 oxidation state K.

Fig. 4(a) and (b) shows the room temperature Mössbauer spectra (MS) of KBFN0 and KBFN10, respectively. The asymmetry lines in the spectra suggest the presence of more than one sextet in the samples with different hyperfine fields. The experimental data for the doped system are fitted by using Mosswin software with a superposition of 2 sextets. The isomer shifts and magnetic hyperfine field for the parent sample are found to be 0.19 mm s^{-1} and 30.21 T, respectively. For KBFN10, δ and H_{hf} are 0.22 mm s^{-1} , 0.51 mm s^{-1} and 29.6 T, 47.4 T, respectively. The δ values for the parent sample correspond to the Fe^{3+} high-spin state, and the H_{hf} value suggests a weak ferromagnetic ordering of the system. However, for the doped system, the Fe ion exhibits a mixed valence state of +3 and +2, which is also observed in the XPS results. The increase in the hyperfine field implies a stronger magnetic ordering due to Ni substitution, and Ni may disrupt the canting spin structure or enhance the coupling between Fe and Ni. The quadrupole shift of KBFN0 decreases with Ni substitution due to local electronic and lattice asymmetry, which reveals FeO_4 tetrahedral distortion in doped samples that form different electric field gradients.²¹ The difference in the hyperfine field and QS can be attributed to changes in the environment of the Fe ion, which confirms the destruction of the antiferromagnetic canting spin structure due to lattice distortion by Ni doping.²²

3.3 Magnetic study

Ni^{2+} is magnetic and is expected to change the ground state WFM ordering of $KBiFe_2O_5$, which typically arises from the

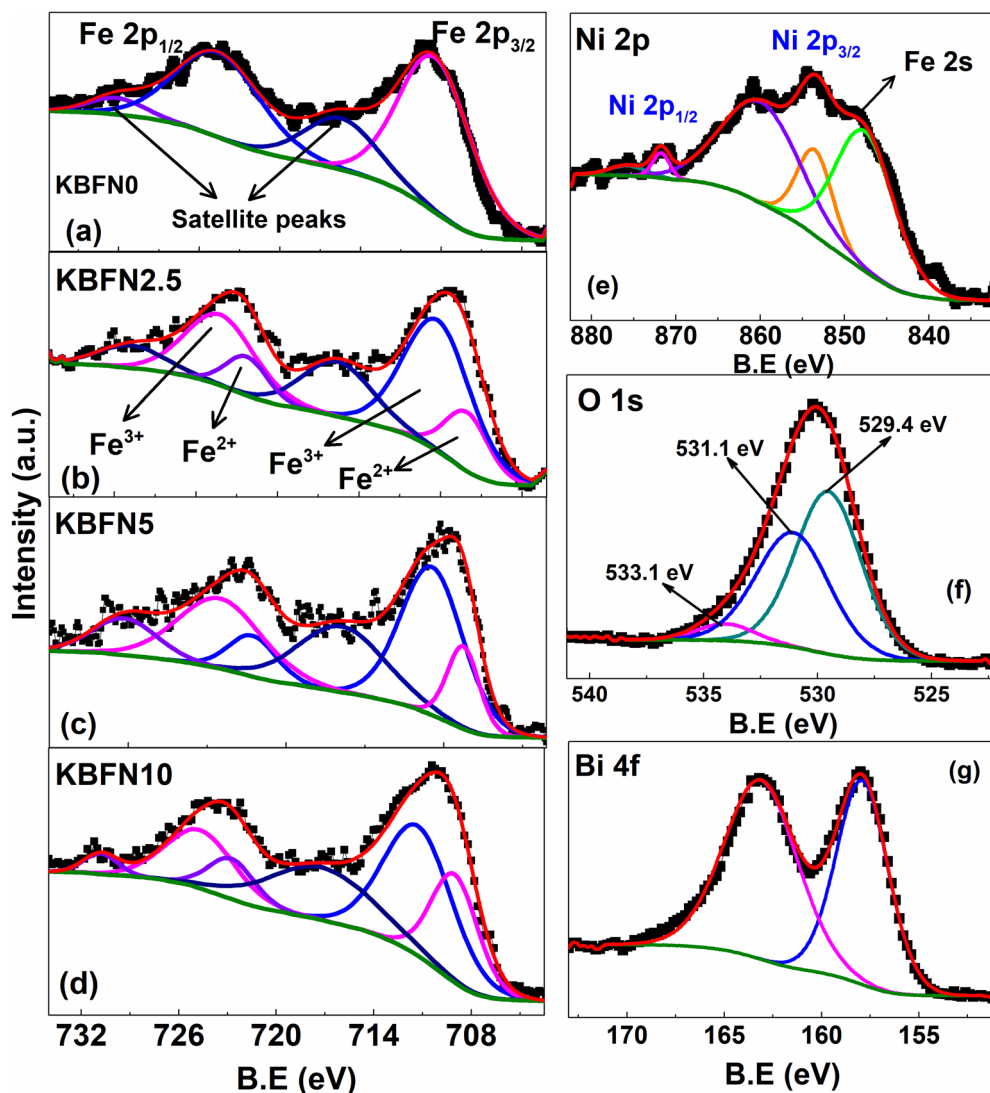


Fig. 3 (a)–(d) XPS spectra of Fe 2p for KBFN0–10 and (e)–(g) high resolution spectra of Ni 2p, O 1s and Bi 4f, respectively, for KBFN10.

uncompensated spins of the Fe³⁺ ion. To investigate this effect, magnetization (M) vs. T is measured in a range of 10 K–850 K under different applied fields. The M vs. T data above room temperature for all the samples are shown in Fig. 5(a)–(d).

As shown in Fig. 5(a), for KBFN0, M starts increasing with T and reaches a maximum value at around 780 K, after which it decreases.²³ Additionally, at 2 kOe, a prominent broad hump is observed around 590 K, which may correspond to a magnetic transition (T_N),^{7,15} although it is not much prominent at lower fields. This magnetic transition is also accomplished by an anomaly in the differential scanning calorimetry (DSC) data of the sample (not shown here), which suggests the possibility of a phase change or order–disorder transition over this T . This type of transition is also visualized in Eu and Co-doped BiFeO₃.^{15,24} By substituting a dilute amount ($x = 0.025, 0.05$ and 0.1) of Ni, the overall magnetic behavior changes, and M starts to decrease with an increase in T and shows a sharp drop at 790 K, 797 K and 815 K, respectively (see Fig. 5(b)). For $x = 0.025$, the magnetic transition T_N is also observed around 590 K, although

it is less prominent (lower inset of Fig. 5(b)). However, this transition is suppressed for higher Ni concentrations and the systems become more ferromagnetic in nature. Furthermore, in all the systems, the FM to PM transition occurs at around 780 K and is well-matched with the recent literature.^{12,15} Upon Ni²⁺ doping, the decrease in the Fe–O–Fe bond angle (away from 180°) weakens the AFM ordering and strengthens the FM ordering between Fe–O–Fe and Fe–O–Ni, thereby increasing the magnetic transition temperature.²⁵

To determine whether any magnetic interactions exist in the PM regions, inverse susceptibility χ^{-1} is measured as a function of T and is shown in the upper inset of Fig. 5(b). In the paramagnetic region, the χ^{-1} vs. T follows the Curie–Weiss (C–W) law $\chi^{-1} = (T - \theta_p)/C$, where θ_p is Weiss temperature and C is the Curie constant. However, for all the samples, χ^{-1} deviates from the linear behaviour and shows a downward curvature, which implies that short-range FM interactions set in in the PM regions.²⁶ The magnetic contribution of Ni ions can be estimated by evaluating the effective magnetic moment

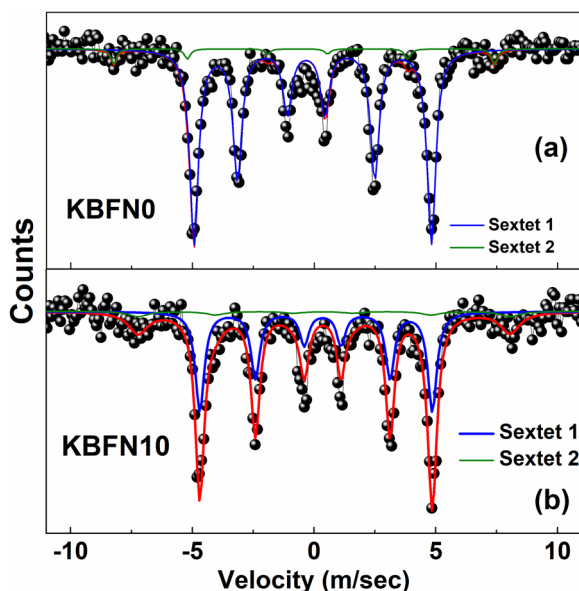


Fig. 4 Room temperature Mössbauer spectra of (a) KBFN0 and (b) KBFN10.

(μ_{eff}) for KBFN0-10 using the formula $C = N_A \mu_{\text{eff}}^2 / 3K_B$.²⁵ The effective magnetic moment is found to be $4.42\mu_B$, $4.04\mu_B$,

$3.72\mu_B$, and $2.61\mu_B$. Upon Ni^{2+} substitution at the Fe^{3+} site, the μ_{eff} decreases. Ni^{2+} has a lower spin-only magnetic moment ($\sim 2.83\mu_B$) compared to the Fe^{3+} ion ($\sim 5.0\mu_B$), and thus when Fe ions are replaced by Ni, it results in a decrease in effective magnetic moment.

However, below 300 K, the system exhibits distinctly different behavior. Here, the M is measured in three different protocols: zero-field cooled (ZFC), field-cooled cooling (FCC) and field-cooled warming (FCW). As shown in Fig. 5(a), ZFC and FC overlap and increase as the T is lowered, suggesting a WFM behavior for KBFN0.²⁴ This behavior is likely due to the uncompensated spins of Fe^{3+} ions in the FeO_4 tetrahedra. However, with Ni substitutions at $x = 0.025$ and 0.05 , the behavior of ZFC is equivalent to either FCC or FCW, with a small change in the magnetization value at lower temperatures. However, a significant bifurcation of ZFC from FC (Fig. 5(d)) shows a mixed state acquired by the system even at low T . Additionally, a minor thermal hysteresis is also seen in the FCC and FCW curves of KBFN10 in Fig. 5(d), which signifies a different magneto-thermodynamic behaviour of the system. Apart from this, ZFC shows a non-monotonic behavior up to 200 K, followed by a small hump (arrow mark) in Fig. 5(d) for KBFN10. These characteristics, which feature in the magnetization, may be linked to a non-ergodic disorder magnetic state

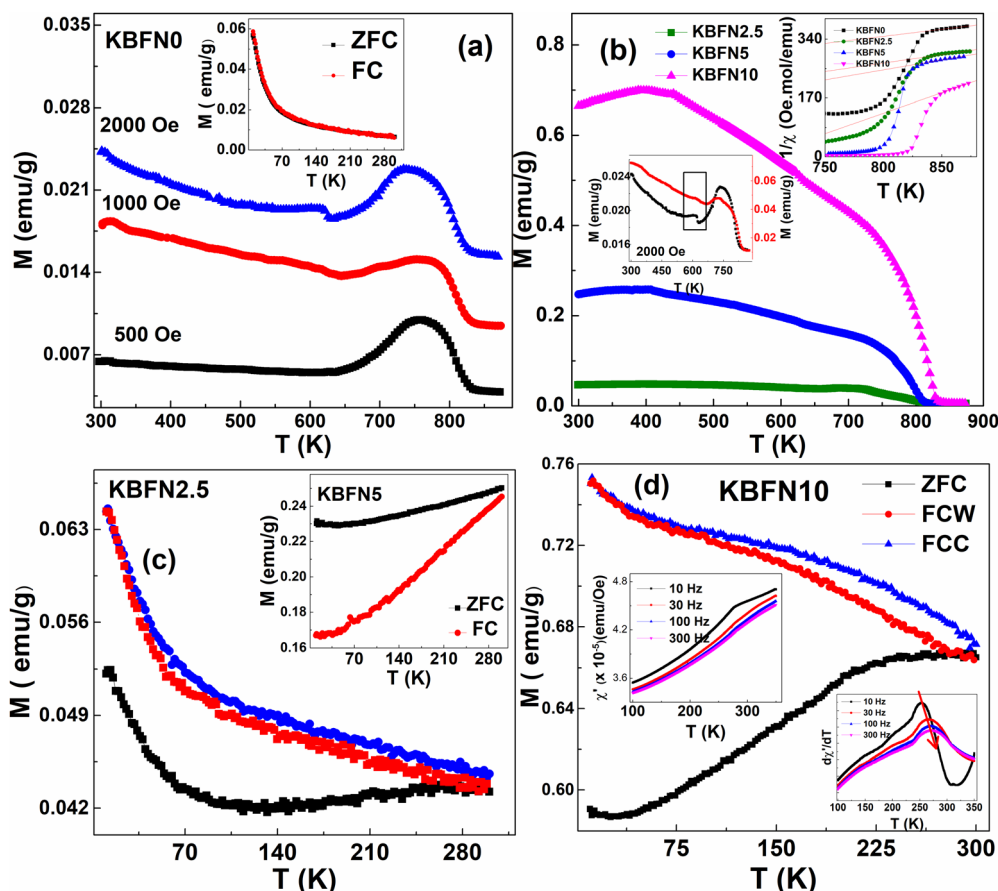


Fig. 5 (a)–(d) M vs. T of KBFN0-10 at different representative fields. Insets: (a) ZFC–FC of KBFN0, (b) upper: Curie–Weiss fits, lower: M vs. T for KBFN0 and 2.5 at 2 KOe, (c) ZFC–FC of KBFN5 and (d) upper: AC- χ , lower: derivatives of AC- χ vs. T at different frequencies for KBFN10.

around 250 K.^{24,27} The irreversibility T (T_{irr} , where ZFC starts bifurcating from FC) of KBFN0-10 is expected to be far above room T ; hence, the magnetic transition is above room temperature for all samples.

In order to confirm the disorder magnetic state in the temperature-dependent magnetic measurement data, AC susceptibility measurement was carried out at different frequencies at an ac field 8 of Oe, as shown in upper inset of Fig. 5(d). The real part of AC susceptibility (χ') exhibits a subtle cusp or inflection point at around 250 K, and this peak shifts with frequency; therefore, we have taken the derivative of χ' (lower inset of Fig. 5(d)). These inflection points are even more distinguishable as peaks in the derivative of χ' , and the corresponding peaks shift towards higher temperatures with increasing frequency, which suggests a glassy behaviour acquired by the sample. To distinguish the observed spin dynamics behaviour of the sample, $\delta T_f = \frac{\Delta T_f}{T_f \Delta \log f}$ is estimated,²⁸ where δT_f represents the relative shift of the peak position with respect to frequency. Generally, for a spin glass system, $\delta T_f = 0.005$ – 0.01 ; for cluster glass, this value should be in the range of 0.03 – 0.08 ; and for a superparamagnetic system,

the value is >0.1 .²⁹ For KBFN10, the calculated value of $\delta T_f \sim 0.067$ lies within the range of cluster glass-like behaviour.

A more detailed analysis of the magnetic phase transformation from WFM to higher order FM due to Ni doping is carried out through isothermal magnetization measurement at a few selected T values (see Fig. 6). As shown in Fig. 6(a), at room T and several other lower temperatures, the characteristics of M vs. H resembles that of a WFM (sigmoid shaped) with a minimal H_c .

The maximum magnetization is mainly due to the canted antiferromagnetic ordering of Fe^{3+} ions in FeO_4 tetrahedra, and the overall magnetism arises from the exchange interactions between the spin-polarized electrons of Fe^{3+} ions and the neighboring Fe^{3+} ions through oxygen. However, for KBFN2.5, a clear hysteresis with a detectable H_c is obtained upon lowering T . This hysteresis becomes more prominent for KBFN10 (Fig. 6(c)) and resembles that of an FM behavior; however, the saturation is yet to be achieved in the available field range. Here, it is also worth noting that above room temperature (as shown in the inset of Fig. 6(a)), due to thermal fluctuations, the canting angle increases, which in turn increases the magnetization. This supports our earlier assertion regarding the AFM

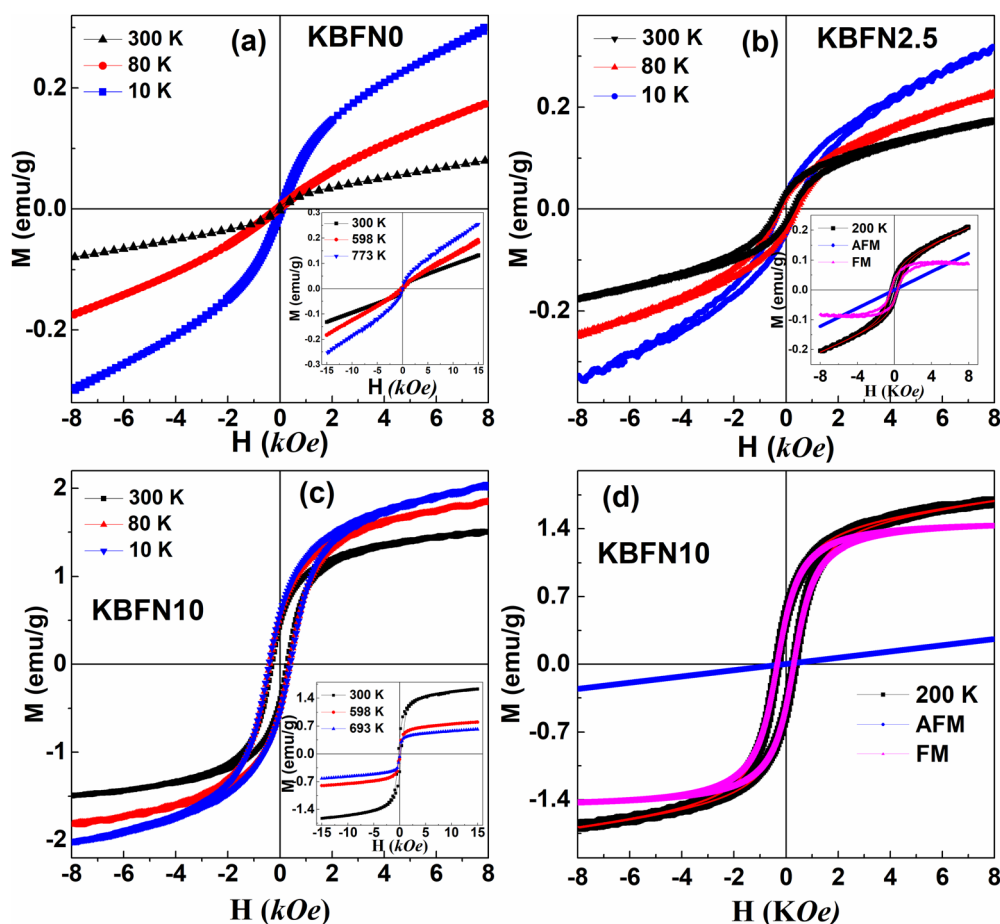


Fig. 6 (a)–(c) Isothermal magnetization for KBFN0-10 and (d) AFM–FM fractions vs. H for KBFN2.5. Inset: (a) and (c) M vs. H at a few selected temperatures for KBFN0 and 10 and (b) AFM–FM fractions vs. H for KBFN2.5.

nature of the parent sample. With Ni incorporation ($x = 0.10$), the behavior of the M - H loop changed, and at room T , the magnetization increases as compared to the parent compound and approaches saturation (inset of Fig. 6(c)). However, the maximum magnetization decreases with increasing T , which signifies ferromagnetic behavior.

Furthermore, the non-attainment of the saturation value for the FM phase in Ni-substituted systems may be associated with the untransformed fraction of AFM coupling among Fe ions coexisting with the FM coupling of Fe-Ni ions.³⁰ Thus, it becomes imperative to estimate the fractions of both the magnetic phases. The FM and AFM contributions to M can be extracted by fitting the M - H loop using eqn (1),³¹

$$M(H) = \left[2 \frac{M_{\text{FM}}^{\text{S}}}{\pi} \tan^{-1} \left\{ \left(\frac{H \pm H_{\text{Ci}}}{H_{\text{Ci}}} \right) \tan \left(\frac{\pi M_{\text{FM}}^{\text{R}}}{2 M_{\text{FM}}^{\text{S}}} \right) \right\} \right] + \chi_{\text{M}} H \quad (1)$$

where M_{FM}^{S} : ferromagnetic saturation magnetization, M_{FM}^{R} : ferromagnetic remnant magnetization, H_{Ci} : intrinsic coercivity, and χ is the antiferromagnetic or paramagnetic susceptibility (see inset of Fig. 6(b) for KBFN2.5 and Fig. 6(d) for KBFN10). Here, the first term is due to the FM contribution, and the second term is due to the PM/AFM contribution. Using this method, at 200 K, the FM fraction for KBFN2.5 is 43.61%, whereas for KBFN10, this fraction increases to 80.45%, indicating a dominance of FM ordering over AFM with Ni substitution, which favors the appearance of the CG phase in the system.^{32–34} Moreover, the maximum magnetization (M_{s}) at room T increases from 0.12 emu g^{-1} to 1.69 emu g^{-1} for $x = 0.10$ Ni, which is nearly 15 times larger than that of the parent compound. Similarly, KBFN0 shows a very small but finite H_{c} at

10 K, and this value is further enhanced to 430 Oe by substituting Ni ($x = 0.10$).

This significant change in magnetization due to Ni substitution in KBiFe_2O_5 is as follows: as mentioned earlier, Ni^{2+} reduces Fe^{3+} to Fe^{2+} , which could lead to multiple interactions among the magnetic ions. Initially, the Ni^{2+} incorporation leads to lattice distortion (increase in the Fe-O bond length and decrease in the bond angle), which increases the tilting angle away from 180° , in turn leading to suppressing the AFM interaction of the $\text{Fe}^{3+}-\text{O}^{2-}-\text{Fe}^{3+}$ chain and favours FM interactions. Additionally, considering the 15-fold change in the magnetic moment as compared to the parent system, the interactions, including $\text{Fe}^{3+}-\text{O}^{2-}-\text{Ni}^{2+}$, $\text{Fe}^{3+}-\text{O}^{2-}-\text{Fe}^{2+}$, also contribute to the overall change in magnetization of the Ni-doped KBiFe_2O_5 , which is otherwise a weak ferromagnetic compound.^{28,35}

3.4 Dielectric study

To get insight into the conduction process and ferroelectric ordering if any in KBF due to Ni substitutions, dielectric constant (ϵ') and loss ($\tan \delta$) are measured in a wide temperature range of 100 K–790 K. As shown in Fig. 7(a)–(f) and Fig. S3(a)–(d) (ESI[†]), with an increase in frequency, both ϵ and $\tan \delta$ exhibit a similar trend, which can be ascribed to the space charge relaxation effect. At low-frequency regions, space charges follow the direction of the applied electric field, whereas in the high-frequency region, these space charges do not undergo relaxation owing to time constraints, resulting in a decrease in the dielectric value.³⁶

A characteristic hump observed at around 560 K in both ϵ' and $\tan \delta$ (as shown in Fig. 7(d) and the upper inset of Fig. 7(a)) may signify the dielectric anomaly in the vicinity of magnetic transitions, which lead the KBiFe_2O_5 to a magneto electrically

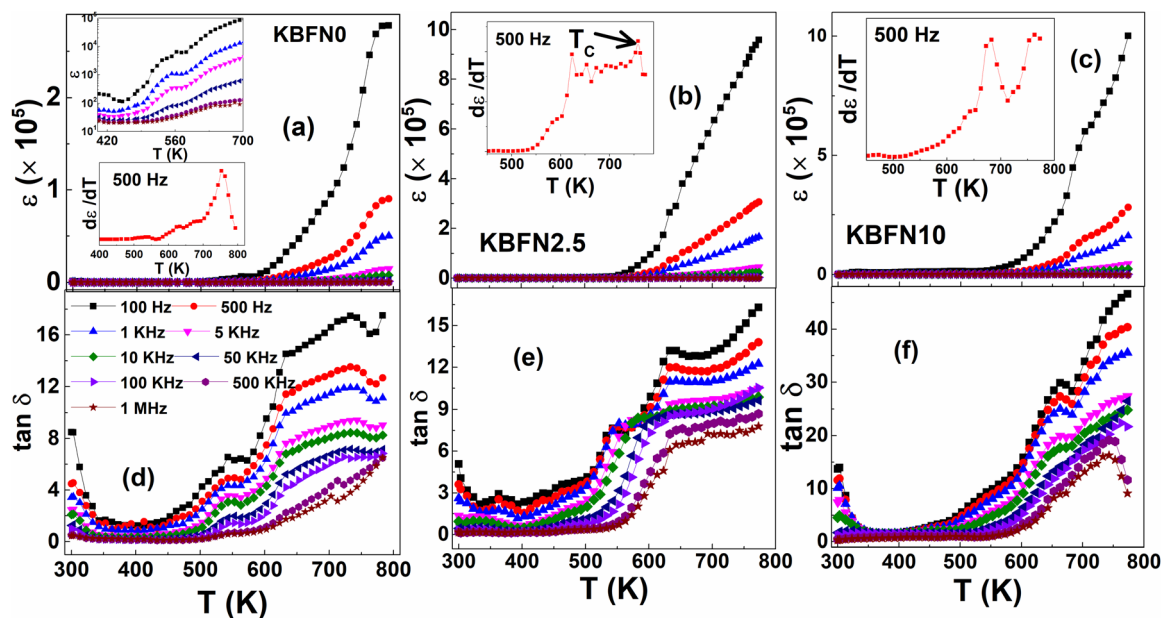


Fig. 7 (a)–(f) Dielectric permittivity and dielectric loss vs. T for KBFN0–10. Inset of (a)–(c); $d\epsilon/dT$ vs. T . Upper inset of (a) is the magnified view in the range of 400 K–700 K.

ordered system.³⁷ Furthermore, after this anomaly, both ϵ and $\tan \delta$ increase with an increase in T , which is attributed to the increase in the dissociation of charge carrier aggregation, thereby enhancing space charge polarization and conductivity.³⁸ The ferroelectric phase transition is, however, detected through the derivative of ϵ with respect to T , and a noticeable change at around 753 K is observed for KBFN0. This change also occurs at 758 K, 763 K and 764 K for KBFN2.5, KBFN5 and KBFN10, respectively, which corresponds to the maximum dielectric loss as in Fig. 7(d)–(f). Since Fe^{3+} is reduced to Fe^{2+} ion with Ni^{2+} doping, it increases the fraction of charge carriers and the charge carrier hopping between Fe^{3+} and Fe^{2+} , allowing the dielectric order to persist at higher temperatures. Here, it is noted that this transition T is also coinciding with the maximum magnetization value (~ 780 K) in the M – T curve as well as with the DSC results of the systems (data not shown here), in which an endothermic peak is observed at 757 K. With Ni, the reduction of Fe^{3+} to Fe^{2+} ion in turn leads to an increase in the number of charge carriers, resulting in an increase in ϵ' .

Furthermore, the features of $\epsilon'(T)$ and $\tan \delta(T)$ are noteworthy once the temperature is below 300 K. The influence of Ni on the dipolar relaxation, as well as dielectric features on KBF is determined by analyzing the $\epsilon'(T)$, $\tan \delta(T)$ in a range of 150 K–300 K (see Fig. 8(a)–(f) and Fig. S3(c) and (d), ESI†). It is found that the dielectric behavior of the parent sample differs from that of the doped system. At low temperatures, $\epsilon'(T)$ remains temperature-independent since the thermal energy is insufficient for the movement of charge carriers, which results in a small variation in the dielectric value in this T range. Conversely, with elevated T , the thermal motion of dipoles increases, resulting in a rise in dielectric constant (for KBFN0 ~ 175 K). With Ni incorporation, the shift in the onset of dielectric permittivity increases from 175 K to 230 K (for

KBFN10) (Fig. 8(b) and (c) and Fig. S5, ESI†), which is attributed to an increase in the number of mobile charge carriers; hence, more thermal energy is needed for the alignment of dipoles in the direction of the applied electric field. Moreover, ϵ' shows a dispersion behavior while a relaxation peak appears in $\tan \delta$ around the dispersion region of $\epsilon'(T)$. Normally, for a single relaxation process, the maximum dielectric loss occurs when the product of the angular frequency ($\omega = 2\pi f$) and relaxation time (τ) becomes unity. The relaxation peak appears at 200 K (200 Hz) for the parent compound, while it is shifted to 262 K (200 Hz) for KBFN10. This thermally activated relaxation behavior is explained through activation energies, which are calculated using the Arrhenius equation;³⁹

$$\tau = \tau_0 \left(\frac{E_a}{eK_B T} \right) \quad (2)$$

where τ is the relaxation time ($1/2\pi f$), E_a is the activation energy of the dielectric relaxation process, and K_B denotes the Boltzmann constant. The slope of the linear fitting of the τ vs. $1000/T$ yields the activation energy, as shown in the inset of Fig. 8(f). The activation energies are calculated to be (0.208 ± 0.011) eV, (0.243 ± 0.001) eV, (0.245 ± 0.005) eV and (0.331 ± 0.022) eV for KBFN0–10, respectively. It is found that the activation energies increase with increasing Ni.

More detailed investigations regarding the relaxation and conduction mechanisms and frequency-dependent electric modulus (imaginary modulus $M'' = \frac{\epsilon''}{\epsilon'^2 + \epsilon''^2}$, where ϵ' and ϵ'' are the real and imaginary parts of dielectric permittivity) were carried out as they have the ability to suppress the surface electrode effect⁴⁰ and are shown in Fig. 9(a)–(d). Similar to permittivity, relaxation peaks appear in M'' , indicating a

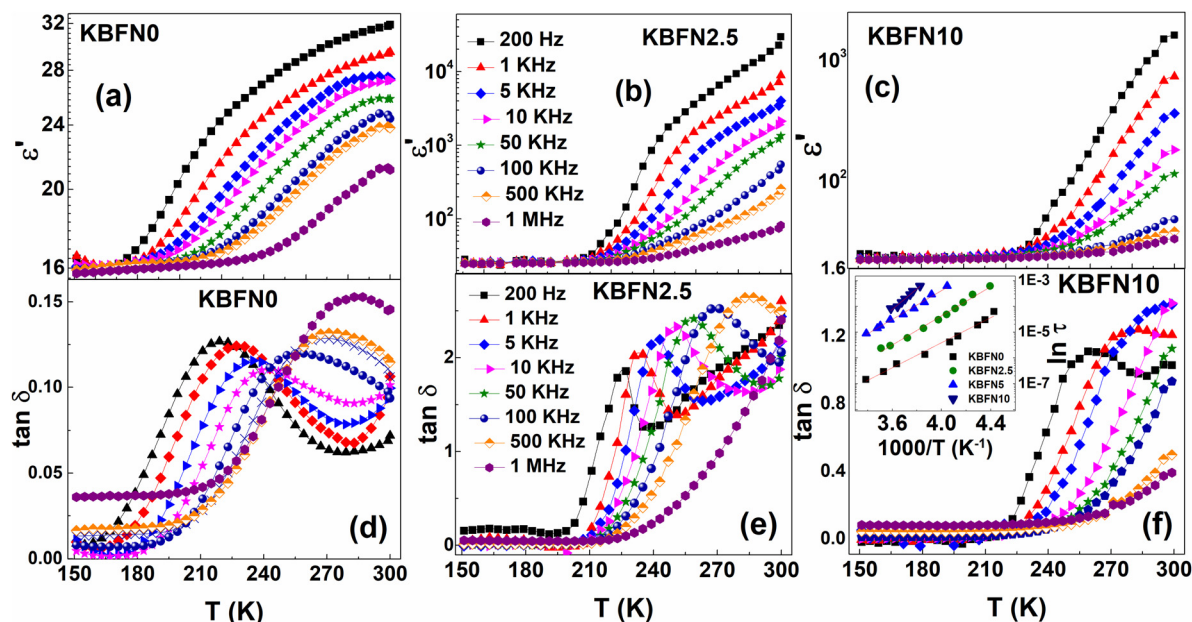


Fig. 8 Temperature-dependent dielectric constant and dielectric loss for (a) and (d) KBFN0, (b) and (e) KBFN2.5 and (c) and (f) KBFN10, respectively. Inset of (f): relaxation time vs. inverse of T for KBFN0–10 deduced from $\tan \delta$.

combined contribution from the grains and grain boundaries. The relaxation peak appears when the hopping frequency is synchronized with the applied electric field. In general, in the low-frequency region, charge carrier hopping from one region to another is long-range hopping, while above the peak maxima, the hopping is however, short-range and confined to a potential well.⁴¹ The relaxation peaks are found to shift towards higher frequencies with increasing T . As the T increases, the mobility of the thermally activated charge carriers increases; thus, the charge carriers relax at the high-frequency region, resulting in peak shifting.⁴² However, the peak at 220 K is shifted towards the lower frequency side (16 614 Hz for KBFN0, 2460 Hz for KBFN2.5, 597 Hz for KBFN5 and 205 Hz for KBFN10, respectively), which indicates an increase in relaxation time and a decrease in the mobility of charge carriers due to Ni substitutions.

The relaxation mechanism is further quantified by estimating E_a using the Arrhenius equation (as in Fig. 9(d)). The calculated E_a values are (0.201 ± 0.005) eV, (0.293 ± 0.014) eV, (0.301 ± 0.012) eV and (0.320 ± 0.008) eV for KNFN0-10, respectively. Ni doping hinders the mobility of charge carriers, requiring additional energies to overcome the potential barrier

for the hopping process and facilitate the relaxation process, leading to an increase in activation energy. Moreover, the proximity in activation energy values from the $\tan \delta(T)$ and $M''(f)$ indicates that similar types of charge carriers govern the relaxation phenomena and conduction process.

To obtain a clear notion of the influence of Ni on the magnetic and electric behavior of KBiFe_2O_5 , the magnetic and electric order parameters of all the compositions are tabulated in Table 2.

From this table, it is observed that, with Ni doping, the M_s or even T_C increases while HC first increases and then slightly decreases while the activation energies continue to increase. The reason for this behavior has already been discussed in their respective sections.

3.5 Impedance study

To acquire detailed information about the contribution of grain and grain boundary and various relaxation mechanisms with Ni substitution, Nyquist plots (Z' vs. Z'' , where Z' and Z'' denote real and imaginary parts of impedance spectroscopy) were analysed at some selected temperatures and shown in Fig. 10(a)–(d). In these plots, each semicircle represents its

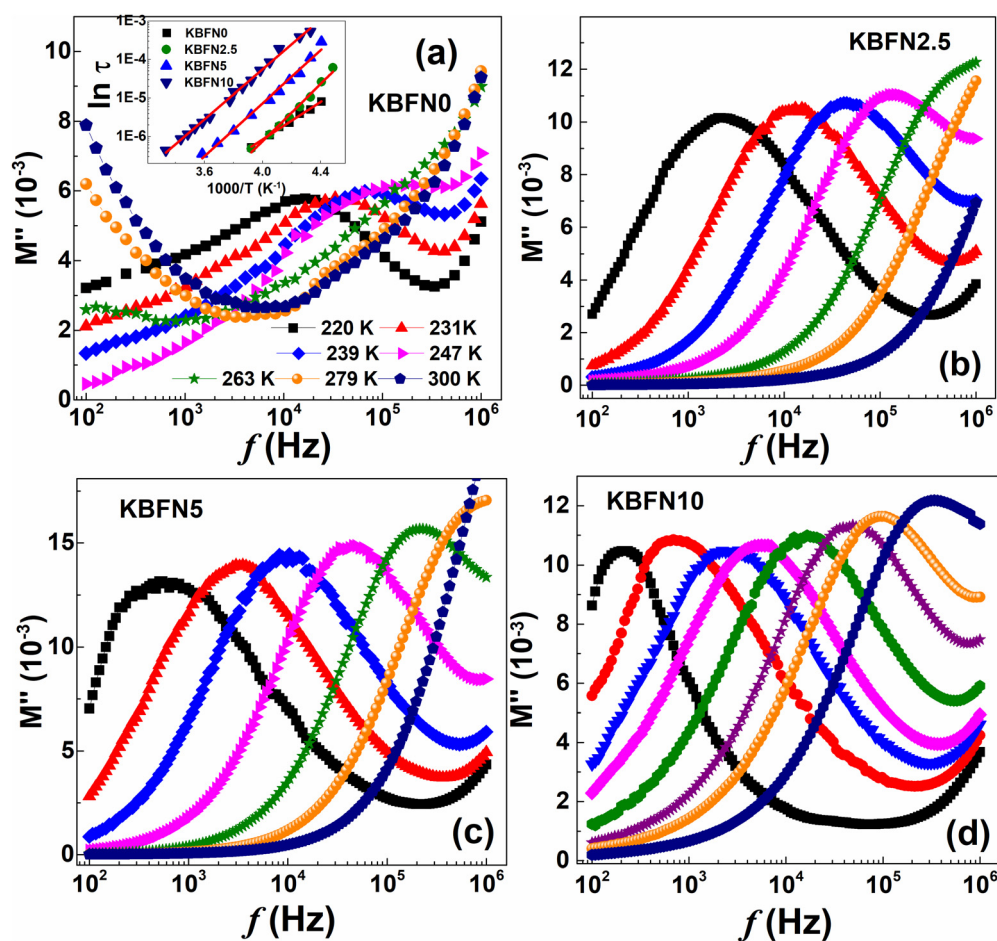


Fig. 9 Frequency-dependent imaginary part of the modulus for (a) KBFN0 (b) KBFN2.5 (c) KBFN5 and (d) KBFN10; inset of (a): relaxation time vs. inverse of T for KBFN0-10 from $M''(f)$.

Table 2 Magnetic and dielectric parameters with different Ni concentrations in $\text{KBiFe}_{2-x}\text{Ni}_x\text{O}_5$

$\text{KBiFe}_{2-x}\text{Ni}_x\text{O}_5$	KBFN0	KBFN2.5	KBFN5	KBFN10
M_s (emu g^{-1}) (300 K)	0.12	0.27	0.78	1.69
H_C (Oe)	107	386	473	430
μ_{eff} (μ_B)	4.42	4.04	3.72	3.61
T_C (K)	753	758	763	764
E_a (eV) (from $\tan \delta$ vs. T)	0.208	0.243	0.245	0.331
E_a (eV) (from M'' vs. f)	0.201	0.293	0.301	0.320

corresponding type of relaxation mechanism in the sample and shows the contributions of grain (high-frequency domain), grain boundary (mid-frequency) and electrode effect (low frequency).⁴⁰ In a single relaxation process, a perfect semicircle will appear with its center on the axis of the real part of the impedance spectra, describing the Debye nature of the sample. However, in real systems, a suppressed semicircle will appear, suggesting non-Debye behavior and the distribution of relaxation time. This can be obtained from the angle between the real axis and the radius of the center of the circle at the high-frequency intercept.

For KBFN0, at 300 K, a high-frequency semicircular arc and a low-frequency arc are observed, attributed to grain and grain boundary relaxation (inset of Fig. 10(a)).

As the temperature is lowered, the high-frequency arc diminishes while the low-frequency arc becomes prominent, indicating that with decreasing temperature, the conduction process is dominated by the grain boundary effect. It is also observed that the diameter of the arc decreases with increasing temperature, which suggests the semiconducting nature of the sample. With Ni substitution ($x = 0.025$), at 300 K, an arc appears in the high-frequency domain, and in the mid-frequency region, a barely visible arc appears and a noticeable upturn is observed in the low-frequency region. The arc at the high-frequency region is due to grains, the region at the mid-frequency is due to grain boundaries, and the low-frequency tail is attributed to trapped charge carriers at interfaces. With lower temperatures, the low-frequency tail grows as a semicircle. With further increasing Ni ($x = 0.05$), both the high-frequency semicircular arc and the low-frequency tail become prominent. This suggests the contribution of grain boundary relaxation or interfacial effect becoming dominant with the incorporation of Ni. When the Ni concentration is further increased, the tail becomes more pronounced in the low and mid-frequency regions, with a flattened arc or shifting of the arc beyond the frequency window towards high frequencies, which confirms the dominance of the grain boundary and electrode effects. This is because Ni^{2+} increases the accumulation of charge

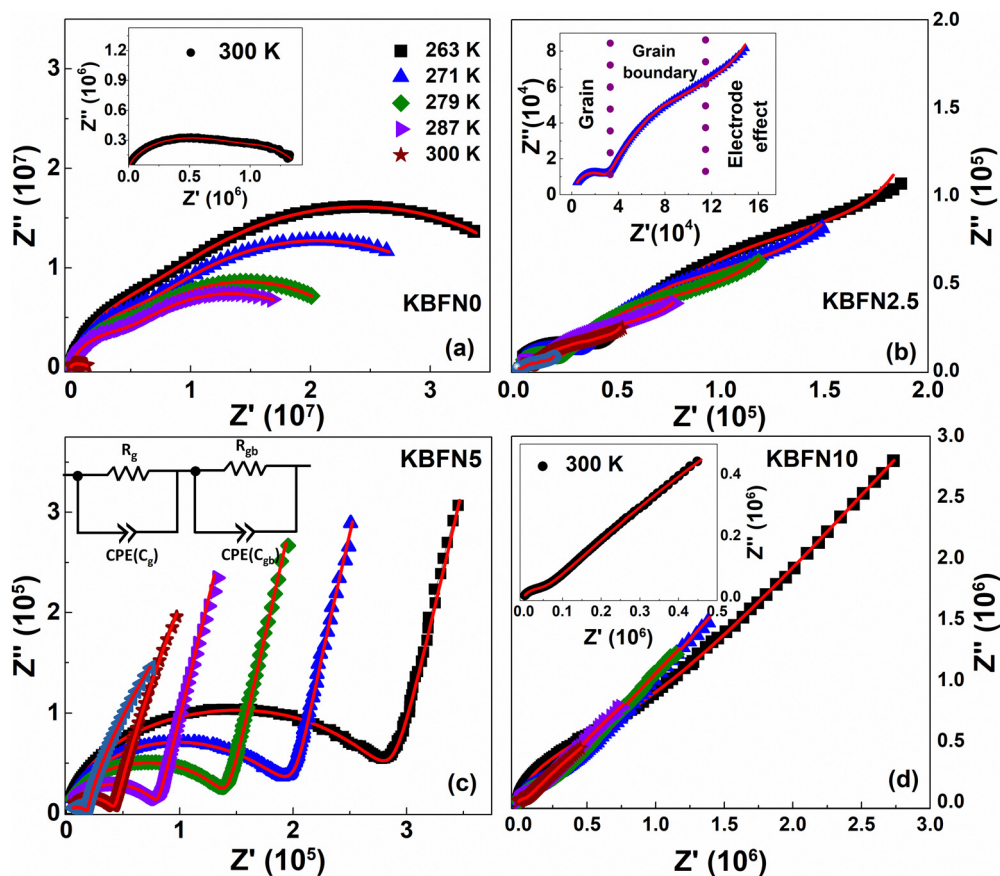


Fig. 10 Cole–Cole plots of (a) KBFN0 (b) KBFN2.5 (c) KBFN5 and (d) KBFN10; inset of (a) Cole–Cole of KBFN0 at 300 K, (b) Cole–Cole plot with grain, grain boundary and electrode effect, (c) equivalent circuit (d) Cole–Cole plot of KBFN10 at 300 K.

carriers (Ni^{2+} , Fe^{3+} , and Fe^{2+}) at grain boundaries and the electrode interface. This result is consistent with the frequency-dependent electric modulus data, which show that the relaxation shifts towards the low-frequency region with Ni incorporation. The impedance spectra for the samples are analysed using ZSIMPWIN software and fitted with the electrical equivalent circuit of two RQ elements connected in series ($R_g Q_g - R_{gb} Q_{gb}$), as shown in the inset of Fig. 10(d). Here, Q is a constant phase element (CPE), which represents the deviation of capacitance from ideal behavior and is defined as $C = Q_n^{\frac{1-n}{n}} R^{\frac{1-n}{n}}$ (n is empirical exponent, ($0 < n < 1$), for ideal capacitor $n = 1$ and for ideal resistor $n = 0$).^{43,44} The fitted value of n decreases with increasing temperature for the grain boundary region for all the compositions. The activation energies are calculated from the grain and grain boundary resistance vs. inverse T , as shown in Fig. S4(a)–(d) (ESI[†]), using the relation $R_{g,gb} = R_0 \exp(E_a/K_B T)$. The activation energies are found to increase from 0.15 eV to 0.29 eV and 0.19 eV to 0.31 eV with increasing Ni concentration for both the grain and grain boundary region, respectively.

4. Conclusion

To summarize, a series of Ni-doped $\text{KBiFe}_{2-x}\text{Ni}_x\text{O}_5$ ($x = 0, 0.025, 0.05$, and 0.1) samples were synthesized using a solid-state method. All the samples are crystallized in a monoclinic structure with a $P2/c$ space group. A mixed valence state of Fe (Fe^{2+} and Fe^{3+}) is found in the Ni-doped system. The parent system exhibited an antiferromagnetic transition around 590 K, which is then suppressed by Ni and transformed into a ferromagnetic state. The thermomagnetic irreversibility predicts a cluster glass-like state well below room temperature, which can be attributed to the competition among the two magnetic phases. This glassy state is then probed through frequency-dependent AC susceptibility analysis. A fifteen-fold increase in the maximum magnetization is associated with the weakening of the AFM interaction of Fe^{3+} and the subsequent appearance of ferromagnetic ordering among the magnetic ions through ligands, such as $\text{Fe}^{3+}-\text{O}^{2-}-\text{Ni}^{2+}$, $\text{Fe}^{3+}-\text{O}^{2-}-\text{Fe}^{2+}$, and $\text{Fe}^{3+}-\text{O}^{2-}-\text{Fe}^{3+}$. The dielectric transition around 753 K is slightly shifted with Ni, which is possibly due to the increase in the fraction of charge carriers resulting in a charge carrier hopping between Fe^{3+} and Fe^{2+} , allowing the dielectric order to persist at higher temperatures. Furthermore, the dielectric anomaly around the magnetic transitions suggests a possibility of an intimate correlation among the two contrasting order parameters, which needs to be verified. All the systems exhibited relaxation behavior, and the relaxation peaks shifted towards lower frequencies, while the increase in activation energy with Ni substitution is attributed to a decrease in the mobility of charge carriers. Finally, a significant change in both the magnetic and dielectric properties and subsequent correlations and possible coupling among them makes this modified brownmillerite useful in multifunctional applications.

Author contributions

Payala Sahoo: writing – original draft, methodology, investigation, formal analysis, data curation, conceptualization. Sujata Kumari Ray: methodology, formal analysis. Anupama Pati: methodology. A. K. Sahoo: methodology. Jaspreet Singh: methodology. S. Dash: writing – review & editing, supervision, methodology, investigation, conceptualization.

Conflicts of interest

The authors declare that they have no known competing financial interests or personal relationships that could have appeared to influence the work reported in this paper.

Data availability

The data supporting this study are included in this article and as part of the ESI.[†]

Acknowledgements

The authors would like to acknowledge the MHRD, Govt. of India, for providing the financial support and various experimental facilities. The authors would like to acknowledge UGC-DAE CSR, Indore, for providing the Mössbauer Spectroscopy facilities for this work. Dr V. Raghavendra Reddy, Scientist H, UGC-DAE CSR, Indore, is highly acknowledged for the support in the Mössbauer measurements and subsequent fitting of the data. Dr D. Samal of IOP Bhubaneswar is highly acknowledged for providing the AC-Susceptibility measurements.

References

- 1 S. W. Cheong and M. Mostovoy, Multiferroics: a magnetic twist for ferroelectricity, *Nat. Mater.*, 2007, **6**, 13.
- 2 C. N. R. Rao and C. R. Serrao, New routes to multiferroics, *J. Mater. Chem.*, 2007, **17**, 4931.
- 3 W. Eerenstein N, D. Mathur and J. F. Scott, Multiferroics and magnetoelectric materials, *Nature*, 2006, **442**, 759.
- 4 N. Ortega, A. Kumar, J. F. Scott and R. S. Katiyar, Multifunctional magnetoelectric materials for device applications, *J. Phys.:Condens. Matter*, 2015, **27**, 504002.
- 5 H. D'Hondt, A. M. Abakumov, J. Hadermann, A. S. Kalyuzhnyana, M. G. Rozova, E. V. Antipov and G. V. Tendeloo, Tetrahedral chain order in the $\text{Sr}_2\text{Fe}_2\text{O}_5$ brownmillerite, *Chem. Mater.*, 2008, **20**, 7188.
- 6 R. Preethi V, S. John, G. Bhalerao, B. Gupta, J. Singh and S. Singh, Photoactive brownmillerite $\text{Ba}_2\text{In}_2\text{O}_5$ for photocatalytic degradation of organic pollutants, *Solid State Sci.*, 2020, **109**, 106450.
- 7 G. Zhang, H. Wu, G. Li, Q. Huang, C. Yang, F. Huang, F. Liao and J. Lin, New high Tc multiferroics KBiFe_2O_5 with narrow band gap and promising photovoltaic effect, *Sci. Rep.*, 2015, **3**, 1265.

- 8 M. Zhang, Z. Wang, S. Lin, Y. Wang and Y. Pan, Investigation on a new multiferroic compound KBiFe_2O_5 : structural, optical, electrical and magnetic properties, *J. Alloys Compd.*, 2017, **699**, 561.
- 9 F. Ramezanipour, J. E. Greedan, A. P. Grosvenor, J. F. Britten, L. M. D. Cranswick and V. O. Garlea, Intralayer cation ordering in a brownmillerites superstructure: synthesis, crystal, and magnetic structures of $\text{Ca}_2\text{FeCoO}_5$, *Chem. Mater.*, 2010, **22**, 6008–6020.
- 10 J. F. Lin, S. Speziale, Z. Mao and H. Marquardt, Effect of electronic spin transitions of iron in lower mantle minerals: implications for deep mantle geophysics and geochemistry, *Rev. Geophys.*, 2013, **51**, 244.
- 11 M. A. Jalaja and S. Dutta, Improved ferroelectric properties in KBiFe_2O_5 -polymer composite film, *Ceram. Int.*, 2019, **45**, 10044.
- 12 K. Chandrakanta, R. Jena, D. P. Sahu, S. D. Kaushik and A. K. Singh, Effect of Holmium substitution on magnetic, dielectric, and magnetodielectric properties of polycrystalline KBiFe_2O_5 , *Mater. Res. Bull.*, 2022, **155**, 111947.
- 13 R. Rai and M. Molli, Effect of La doping on structural, magnetic and optical properties of KBiFe_2O_5 , *J. Mater. Sci.: Mater. Electron.*, 2019, **30**, 4318.
- 14 R. Rai and M. Molli, Magnetic, optical and photocatalytic properties of yttrium doped KBiFe_2O_5 , *Appl. Phys. A: Mater. Sci. Process.*, 2019, **125**, 878.
- 15 K. Chandrakanta, R. Jena, P. Pal, M. F. Abdullah, S. D. Kaushik and A. K. Singh, Enhanced magnetic and magnetodielectric properties of Co doped brownmillerite KBiFe_2O_5 at room temperature, *J. Alloys Compd.*, 2021, **886**, 161294.
- 16 R. Babu, R. Koduri, S. Srivathsava and K. V. Ramesh, Investigation of structural, magnetic, and electrical properties of Ru doped brownmillerite oxide: KBiFe_2O_5 , *Mater. Chem. Phys.*, 2022, **280**, 125812.
- 17 J. Young and J. M. Rondinelli, Crystal Structure and Electronic Properties of Bulk and Thin Film Brownmillerite Oxides, *Phys. Rev. B: Condens. Matter Mater. Phys.*, 2015, **92**, 174111.
- 18 B. D. Cullity, *Elements of X-Ray Diffraction*, Addison Wesley Series, Reading, MA, 2nd edn, 1978.
- 19 M. A. Shaida, S. Verma, S. Talukdar, N. Kumar, M. S. Mahtab, M. Naushad and I. H. Farooqi, Critical analysis of the role of various iron-based heterogeneous catalysts for advanced oxidation processes: A state of the art review, *J. Mol. Liq.*, 2023, **374**, 121259.
- 20 V. Biju, Ni 2p X-ray photoelectron spectroscopy study of nanostructured nickel oxide, *Mater. Res. Bull.*, 2007, **42**, 491.
- 21 S. Han and C. S. Kim, Weak ferromagnetic behavior of BiFeO_3 at low temperature, *J. Appl. Phys.*, 2013, **113**, 17D921.
- 22 R. Z. Xiao, T. Hu, X. Yuan, J. J. Zhou, X. Qiang Ma and D. J. Fu, Studies of La- and Pr-driven reverse distortion of FeO_6 octahedral structure, magnetic properties and hyperfine interaction of BiFeO_3 powder, *RSC Adv.*, 2018, **8**, 12060.
- 23 P. Sahoo, S. K. Ray, A. Pati, A. K. Sahoo, S. Chakravarty and S. Dash, Effect of Al substitution on the magnetic, optical and electronic properties of KBiFe_2O_5 brownmillerite, *Solid State Sci.*, 2024, **152**, 107533.
- 24 K. Chakrabarti, K. Das, B. Sarkar, S. Ghosh, S. K. De, G. Sinha and J. Lahtinen, Enhanced magnetic and dielectric properties of Eu and Co co-doped BiFeO_3 nanoparticles, *Appl. Phys. Lett.*, 2012, **101**, 042401.
- 25 R. Ghosh, S. Mishra, A. Barik, M. R. Sahoo, D. Saini, D. Mandal, P. D. Babu, S. D. Kaushik and P. N. Vishwakarma, Sm substitution induced spin reorientation and stabilization of double perovskite structure resulting in enhanced magnetoelectricity in LaYFe_2O_6 , *J. Appl. Phys.*, 2012, **135**, 104101.
- 26 M. Das, P. Sarkar and P. Mandal, Non-Griffiths-like cluster formation in the double-perovskite $\text{Gd}_2\text{CoMnO}_6$: Evidence from critical behavior, *Phys. Rev. B*, 2020, **101**, 144433.
- 27 Y. J. Yoo, J. S. Hwang, Y. P. Lee, J. S. Park, J.-H. Kang, J. Kim, B. W. Lee and M. S. Seo, High ferromagnetic transition temperature in multiferroic $\text{BiFe}_{0.95}\text{Ni}_{0.05}\text{O}_3$ compound, *J. Appl. Phys.*, 2013, **114**, 163902.
- 28 B. Roy and S. Das, Magnetic cluster glass behavior and grain boundary effect in $\text{Nd}_{0.7}\text{Ba}_{0.3}\text{MnO}_3$ nanoparticles, *J. Appl. Phys.*, 2008, **104**, 103915.
- 29 A. Hadded, J. Massoudi, S. Gharbia, E. Dhahri Logoa, A. Tozrib and M. R. Berber, Study of physical properties of a ferrimagnetic spinel $\text{Cu}_{1.5}\text{Mn}_{1.5}\text{O}_4$: spin dynamics, magnetocaloric effect and critical behavior, *RSC Adv.*, 2021, **11**, 25664–25676.
- 30 M. Nadeem, W. Khan, S. Khan, S. Husain and A. Ansari, Tailoring dielectric properties and multiferroic behavior of nanocrystalline BiFeO_3 via Ni doping, *J. Appl. Phys.*, 2018, **124**, 164105.
- 31 S. Tiwary, S. Kuila, M. R. Sahoo, A. Barik, P. D. Babu and P. N. Vishwakarma, Magnetoelectricity in $\text{La}_2\text{NiMnO}_6$ and its PVDF impregnated derivative, *J. Appl. Phys.*, 2018, **124**, 044101.
- 32 B. Ramachandran and M. S. Ramachandra Rao, Low temperature magnetocaloric effect in polycrystalline BiFeO_3 ceramics, *Appl. Phys. Lett.*, 2009, **95**, 142505.
- 33 J. Wu and C. Leighton, Glassy ferromagnetism and magnetic phase separation in $\text{La}_{1-x}\text{Sr}_x\text{CoO}_3$, *Phys. Rev. B: Condens. Matter Mater. Phys.*, 2003, **67**, 174408.
- 34 S. Mukherjee and R. Ranganathan, Static and dynamic response of cluster glass in $\text{La}_{0.5}\text{Sr}_{0.5}\text{CoO}_3$, *Phys. Rev. B: Condens. Matter Mater. Phys.*, 1996, **54**, 9274.
- 35 Q. Yao, C. Tian, Z. Lu, J. Wang, H. Zhou and G. Rao, Antiferromagnetic-ferromagnetic transition in Bi-doped LaFeO_3 nanocrystalline ceramics, *Ceram. Int.*, 2020, **46**, 20472–20476.
- 36 J. C. Maxwell, *Treatise on Electricity and Magnetism*, Clarendon Press, Oxford, 1873.
- 37 M. Kumar and K. L. Yadav, The effect of Ti substitution on magnetoelectric coupling at room temperature in the $\text{BiFe}_{1-x}\text{Ti}_x\text{O}_3$ system, *J. Phys.: Condens. Matter*, 2006, **18**, L503–L508.
- 38 S. Singh, A. Kaur, P. Kaur and L. Singh, High-Temperature Dielectric Relaxation and Electric Conduction Mechanisms in a LaCoO_3 -Modified $\text{Na}_{0.5}\text{Bi}_{0.5}\text{TiO}_3$ System, *ACS Omega*, 2023, **8**, 25623–25638.

- 39 Y. Ben Taher, N. Moutia, A. Oueslatia and M. Gargouri, Electrical properties, conduction mechanism and modulus of diphosphate compounds, *RSC Adv.*, 2016, **6**, 39750–39757.
- 40 T. Lakshmana Rao, M. K. Pradhan, U. K. Goutam, V. Siruguri, V. R. Reddy and S. Dash, Substitution induced magnetic phase transitions and related electrical conduction mechanisms in LaFeO_3 nanoparticle, *J. Appl. Phys.*, 2019, **126**, 064104.
- 41 A. Dhahri, E. Dhahri and E. K. Hlilc, Electrical conductivity and dielectric behaviour of nanocrystalline $\text{La}_{0.6}\text{Gd}_{0.1}\text{Sr}_{0.3}\text{Mn}_{0.75}\text{Si}_{0.25}\text{O}_3$, *RSC Adv.*, 2018, **8**, 9103.
- 42 C. Rayssi, S. E. Kossia, J. Dhahri and K. Khirouni, Frequency and temperature-dependence of dielectric permittivity and electric modulus studies of the solid solution $\text{Ca}_{0.85}\text{Er}_{0.1}\text{Ti}_{1-x}\text{Co}_{4x/3}\text{O}_3$ ($0 \leq x \leq 0.1$), *RSC Adv.*, 2018, **8**, 17139–17150.
- 43 G. Jagadish Kumar and K. Kamala Bharathi, Near-room-temperature magnetocaloric properties at 1.5 T coupled with relaxor dielectric properties in $\text{La}_2\text{CoMnO}_6$ nanoparticles, *J. Phys. Chem. Solids*, 2014, **186**, 111829.
- 44 R. Datta, S. K. Pradhan, S. Majumdar and S. Kumar De, Dielectric and impedance spectroscopy of $\text{Nd}_2\text{CoIrO}_6$ double perovskite, *J. Phys.:Condens. Matter*, 2020, **32**, 495702.